The following article appeared in Journal of Ceramic Processing Research 20 (3): 222-230 (2019); and may be found at:
https://doi.org/10.36410/jcpr.2019.20.3.222

Journal of Ceramic Processing Research. Vol. 20, No. 3, pp. 222~230 (2019)
(Received 11 January 2019, Received in revised form 29 May 2019, Accepted 3 June 2019)

J O U R N A L O F
Ceramic Processing Research

Enhancement of NOx photo-oxidation by Fe-doped TiO_2 nanoparticles

Adriana Martinez-Oviedo[a], Schindra Kumar Ray[a], Gobinda Gyawali[b], Vicente Rodriguez-Gonzalez[c] and Soo Wohn Lee[a,*]

[a]*Department of Environmental and Bio-Chemical Engineering, Sun Moon University, Asan, Chungnam, 31460, Korea*
[b]*Division of Basic Engineering, Sun Moon University, Asan, Korea*
[c]*División de Materiales Avanzados, Instituto Potosino de Investigación Científica y Tecnológica, Camino a la Presa San José 2055 Col. Lomas 4a. sección, C.P. 78216 San Luis Potosí, S.L.P., México.*

Microwave hydrothermal-assisted sol-gel method was employed to synthesize the Fe doped TiO_2 photocatalyst. The morphological analysis suggests anatase phase nanoparticles of ~20 nm with an S_{BET} area of 283.99 m^2/g. The doping of Fe ions in TiO_2 created oxygen vacancies and Ti^{3+} species as revealed through the XPS analysis. The reduction of the band gap (3.1 to 2.8 eV) is occurred by doping effect. The as-prepared photocatalyst was applied for removal of NOx under solar light irradiation. The doping of Fe in TiO_2 facilitates 75 % of NOx oxidation efficiency which is more than two-fold enhancement than the TiO_2 photocatalyst. The possible reason of enhancement is associated with high surface area, oxygen vacancy, and reduction of the band gap. Also, the low production of toxic intermediates, NO_2 gas, is further confirmed by Combustion Ion Chromatography. The mechanism related NOx oxidation by the doped photocatalyst is explained in this study.

Key words: Fe doped TiO_2, Microwave hydrothermal, Sol-gel; DeNOx, NO_2 inhibition.

Introduction

Since the last decade traces of oxides of nitrogen ($NO + NO_2 = NOx$) had been found responsible for atmospheric environmental problems. NOx is part of the gaseous pollutants that receives major attention due to the hazardous impact it has on human health and the environment [1, 2]. The primary route of NOx to enter the atmosphere is from the emission of vehicles and combustion in industries. Although removal and prevention treatments are in practice, the removal of NOx is not successfully achieved. One of the major concerns of these treatments is the production of toxic intermediates such as NO_2 gas [3, 4]. Hence, new eradication methods need to be considered for the effective oxidation of NO.

Photocatalysis is a relatively cheap and novel technique for the decomposition of contaminants in aqueous and gaseous media. The process goes from charge separation to the charge consumption on redox reactions. In general, an electron is excited from the valence band to the conduction band leaving a hole behind. Then, the photoinduced holes can be easily captured by chemisorbed surface hydroxyl to produce hydroxyl radical group $OH^{\bullet}$, while the electrons can be trapped by adsorbed O_2 to produce superoxide radical ion $O_2^{\bullet}$ [5, 6].

Titanium dioxide (TiO_2) has been found to be a good catalyzer because it is chemically stable and ecologically benign. TiO_2 exists in three important polymorphs, rutile, anatase, and brookite but is generally accepted that anatase exhibits a higher photocatalytic activity. The band-gap of TiO_2 anatase is of 3.2 eV. Thus, it is exclusively active for UV light, about 3 % of the solar spectrum. Such disadvantage requires the re-engineering of the band-gap structure to increase the photoactivity of TiO_2 [7, 8].

Different methods have been suggested to reduce the band gap of TiO_2. However, partly substitution of Ti with a transitional metal ion such as Cr, Mn, Cu, Ag, and Fe has proved to have higher photocatalytic activity under visible light owing to a band gap narrowing [9-14]. Among the dopants, Fe shows to be adequate due to the similarities in ionic radii (Fe^{3+}: 0.64 Å and Ti^{4+}: 0.68 Å), which allow effective incorporation in the TiO_2 structure. Furthermore, the energy levels Fe^{2+}/Fe^{3+} can act as electron traps due to the similarity to Ti^{3+}/Ti^{4+} [15, 16].

In the present work, Fe-doped TiO_2 was synthesized by a hydrothermal-assisted sol-gel method. Different concentrations of Fe-doped TiO_2 have been prepared and investigated for their photocatalytic performance on the gaseous media. The designed photocatalyst possesses a perfect combination of electronic and structural properties that facilitate the adsorption of NO gas while inhibiting the production of toxic intermediates such as NO_2.

*Corresponding author:
Tel : +82-41-530-2882
Fax: +82-41-530-2840
E-mail: swlee@sunmoon.ac.kr

Experimental Procedure

Synthesis of the photocatalyst

Titanium (IV) Isopropoxide ($Ti[OCH(CH_3)_2]_4$, Mw = 284.22), and Iron Nitrate ($Fe(NO_3)_3 \cdot 9H_2O$, Mw = 404.00) were purchased from Sigma Aldrich. The materials were analytical grade and used without any further purification. TiO_2 was prepared using a sol-gel hydrothermal-assisted method. First, a required amount of alkoxide was dropped into a solution of distilled water and ethanol for a period of 120 min. The molar ratio was 1:3:8 (alkoxide/ethanol/water). Subsequently, the solution was loaded into microwave irradiation for 240 min at 150 W. Finally, the product was washed with distilled water and dried. The method was revised and modified from previous works [17, 18]. For the Fe-doped TiO_2, a desired amount of $Fe(NO_3)_3 \cdot 9H_2O$ was mixed in the ethanol and water to form molar concentrations of 2, 3, and 4 mole %. The rest of the procedure was followed as mentioned above. The samples were labeled as TF2, TF3, and TF4 respectively.

Characterization method

The crystal phase was determined by X-Ray diffraction using a spectrometer Rigaku D/mas-2200 HR with a CuKα radiation, at a scan ratio of 4°/min. The crystal size was obtained according to the Scherrer formula. Morphological studies were carried out using Field-Emission Scanning Electron Microscopy (FESEM, JEOL-2010). Later, High-Resolution Transmittance Electron Microscopy (HRTEM, JEOL, JIEM-2100F) was utilized to investigate the crystal structure. The Brunauer-Emmett-Teller (BET) surface area (S_{BET}) and pore size distribution were collected from a micrometric ASAP 2020 nitrogen adsorption apparatus. The chemical composition was studied from X-Ray Photoelectron Spectroscopy (XPS) by an XR5 gun -500 μm at 15 kV/ 150 w. To understand the molecular bonds, Raman spectroscopy was performed using confocal μ-Raman System (LabRAM HR800, 532 nm laser). The optical properties were measured using DRS UV-vis absorption spectra using a JASCO, V-570 spectrophotometer. While the indirect band-gap was calculated by the Kubelka-Munk Function.

Photocatalytic measurement

The photocatalytic activity was measured by the removal of NOx gases. An apparatus Horiba APNA-370 was used to monitor the NOx flow. A solar simulator from ABET technologies with a full range wavelength was used as the light source. The experiment was executed with 0.05 g of catalyst dissolved in acetone and evenly dispersed in a sample dish of 50 mm of diameter. After dried, the sample dish was supported in the middle of the reactor. The experiment was fixed in a continuous NO flow to form an initial concentration of ~400 parts per billion (ppb) of NO, ~30 ppb of NO_2, and a relative humidity of ~50%. After a flow stabilization and an adsorption-desorption period of 30 min, the sample was irradiated for 60 min. Measurements were taken at certain intervals of time. Finally, the NO_3^- formation over the catalyzer after used was measured by Combustion Ion Chromatograph (ICS 3000, Dionex).

Results and Discussion

Characterization of the catalyst

Fig. 1 shows XRD patterns of the samples TiO_2, TF2, TF3, and TF4. According to the JCPDS card no. 21-1272, all samples show the representative peaks of anatase phase. The Fe-doped samples present broadening of (101) peak with the decreased peak intensity. This can be attributed to distortions provoked by the addition of foreign ions (Fe) [19]. The ions of iron interact with the TiO_2 alkoxide precursor in the sol step. Later, during the gelation, the Fe ions are able to incorporate in the TiO_2 lattice. The incorporation happens through the substitution of some Ti ions by Fe ions. The substitution is possible as a result of the similar ionic radii [20, 21]. Additionally, the Debye-Scherrer formula ($d = 0.9\lambda/\beta \cos\theta$) was used to determine the size of the crystal. TiO_2 counts with crystallite size of ~12.5 nm, while the samples TF2, TF3, and TF4 are of 8.7, 5, and 7 nm, respectively. The reasons for reduction in crystallite size in samples TF2, TF3, and TF4 are associated with introduction of Fe ions that inhibit the grain growth as well as fast crystallization process [22]. In addition, the low crystallite size of TF3 is related with optimal doping amount of Fe ions in TiO_2 lattice. Furthermore, the crystallite size of TF4 is increased due to exceed of doping level.

The FESEM images from TF2, TF3, and TF4 samples are presented in Fig. 2a, 2b, and 2c, respectively. All the samples consist of irregular sponge-like particles. However, the addition of Fe species produced a reduction

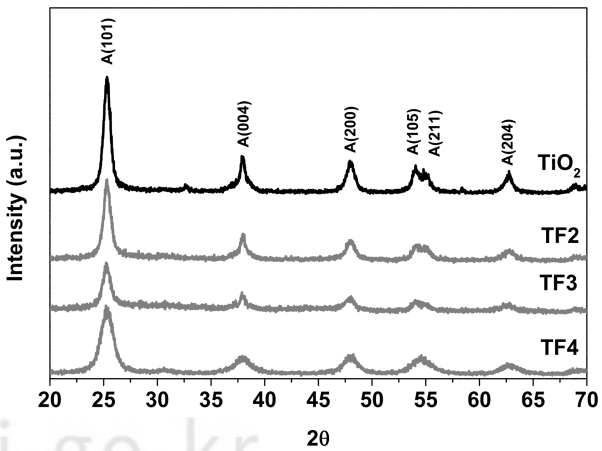

Fig. 1. XRD spectra of the as-synthetized samples.

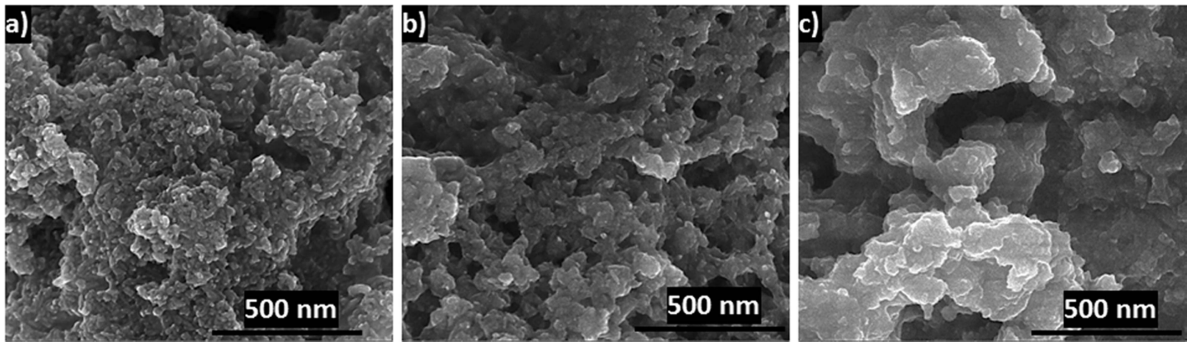

Fig. 2. FESEM images of the samples: (a) TF2, (b) TF3, and (c) TF4.

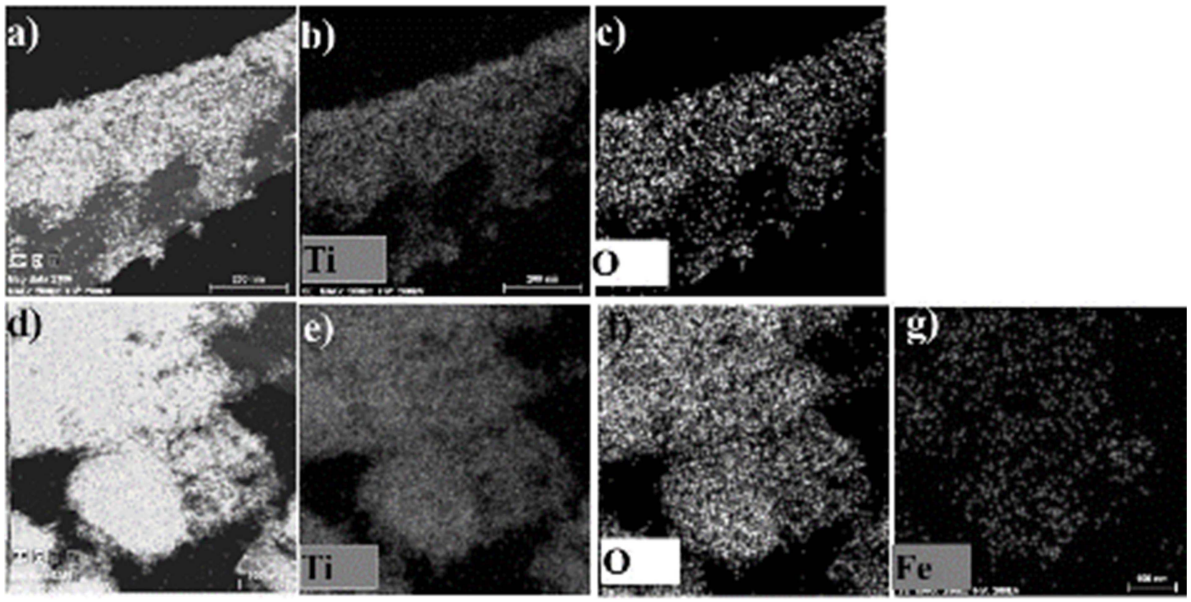

Fig. 3. TEM elemental mapping composition of the samples TiO_2 (a-c), and TF3 (d-g).

on the crystal size and increment of agglomerations. The sample TF4 counts with the highest degree of agglomeration. This is attributed to the accelerated nucleation provoked by the addition of Fe ions that makes the higher saturation resulting smaller crystal size [22]. The nucleation and crystal growth rate show to be dependent on the seed characteristics. This is, the samples with low saturation of TiO_2 and Fe ions (TiO_2 and TF2), the crystal nucleation follows a "primary mechanism". The primary mechanism happens when the solute aggregates overcome the critical size, and the nucleus remains as a crystallite. On the other hand, the supersaturated solutions (TF3 and TF4) have a crystal nucleation through the "second mechanism". This last mechanism is the formation of small particles by the reduction of crystals via breaking mechanisms; abrasion, attrition and fracture [23].

Fig. 3 reveals the TEM elemental mapping of the samples TiO_2 (Fig. 3a, 3b, and 3c) and TF3 (Fig. 3d, 3e, 3f, and 3g). It is confirmed an elemental composition of Titanium and Oxygen in TiO_2. The sample TF3 counts with an elemental composition of Titanium, Oxygen, and Iron. Additionally, HRTEM images (Fig. 4) show that TiO_2 (Fig. 4a) and TF3 (Fig. 4b) have a d-spacing of 0.35 nm, which corresponds to the crystal phase anatase of the plane (101) [7]. It is easy to see that the lattice parameters of the doped-sample remains as the plain TiO_2. This is explain by the similarities of ionic radii found in the Ti ions and Fe ions. Thus, any substitution of Fe ion will keep the same lattice spacing in the crystallite [9]. The same polymorph was confirmed by the solid phase crystallization (SPC) in the anatase phase. This is consistent with the XRD analysis.

Fig. 5 shows the N_2 absorption-desorption isotherms of the TiO_2 and TF3. The surface area, obtained by the BET method, of TiO_2 and TF3 samples are 104 m^2/g and 283.99 m^2/g, respectively. The isotherms represent the relation of N_2 adsorbed vs the relative pressure, which exhibit the fluid-wall interaction and the stability of fluids confined in a pore. According to the IUPAC

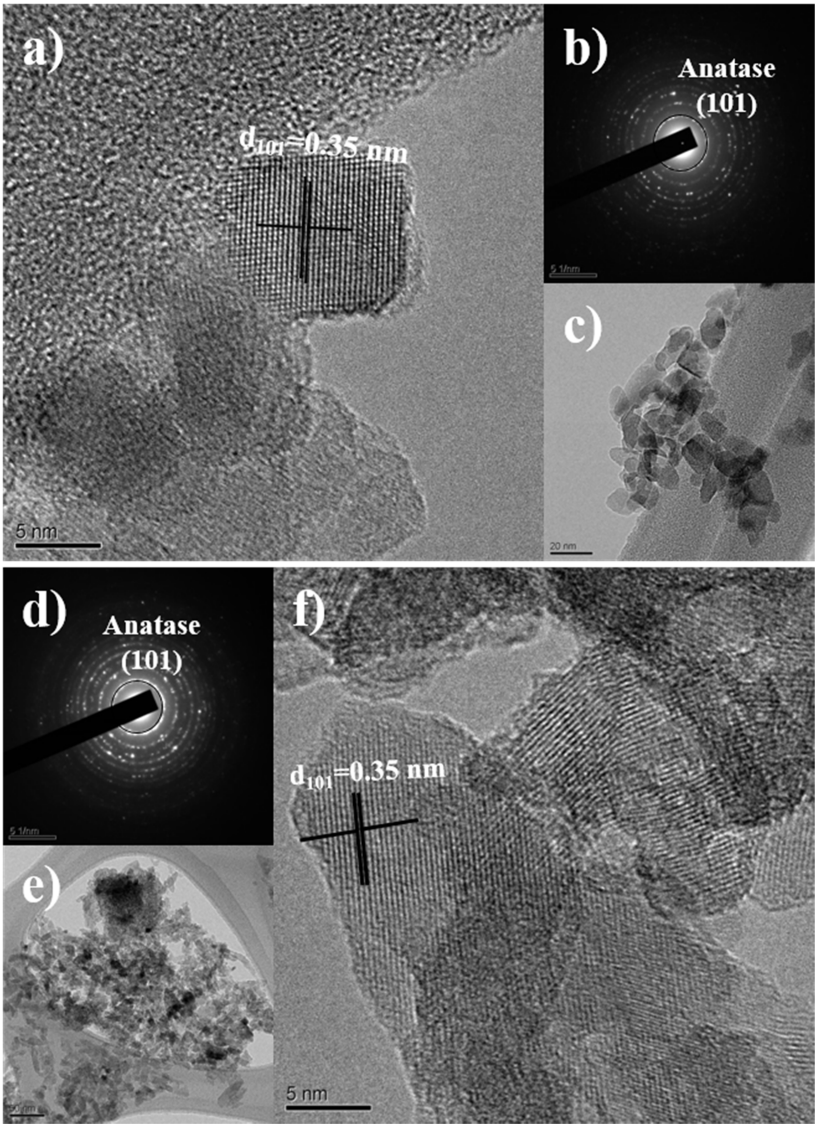

Fig. 4. TEM, HRTEM images and SPD patterns of the samples: (a-c) TiO_2 and (d-f) TF3.

classification, the shapes of the hysteresis loops are of the type H1 for TiO_2 and H3 for TF3 samples. The materials with H1 type are associated with porous structure with narrow distribution of pores. Differently, the Isotherms of type-3 are described by materials with plate-like agglomerations forming slit-shaped pores arrangement [24]. The huge increment of surface area and pore volume are related to the reduction of the crystal size [25]. Furthermore, the corresponding BJH pore volume distribution were 0.196 cm^3/g and 0.20 cm^3/g for TiO_2 and TF3, respectively, which is consistent with the FESEM images.

X-ray photoelectron spectroscopy was utilized to investigate the surface elemental composition of TiO_2 and TF3 samples (Fig. 6). Analysis of the Ti 2p peaks revealed a doublet splitting orbital of Ti $2p_{1/2}$ and Ti $2p_{3/2}$. After a deconvolution, Ti $2p_{3/2}$ at 459.5 eV and 465.3 eV are assigned to the Ti^{4+} state of TiO_2.

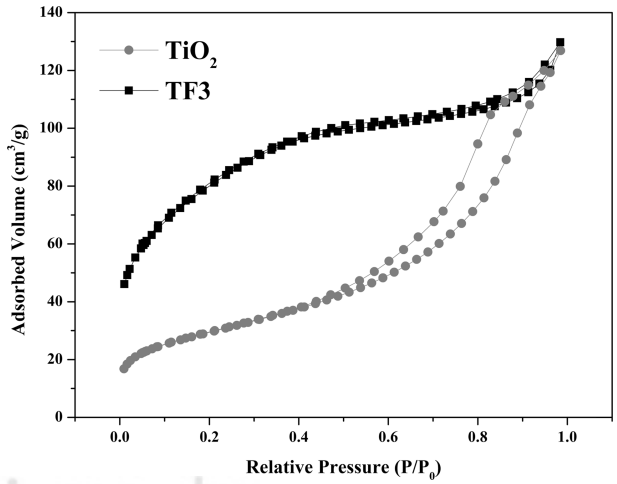

Fig. 5. N_2 adsorption-desorption isotherms of the samples TiO_2 and TF3.

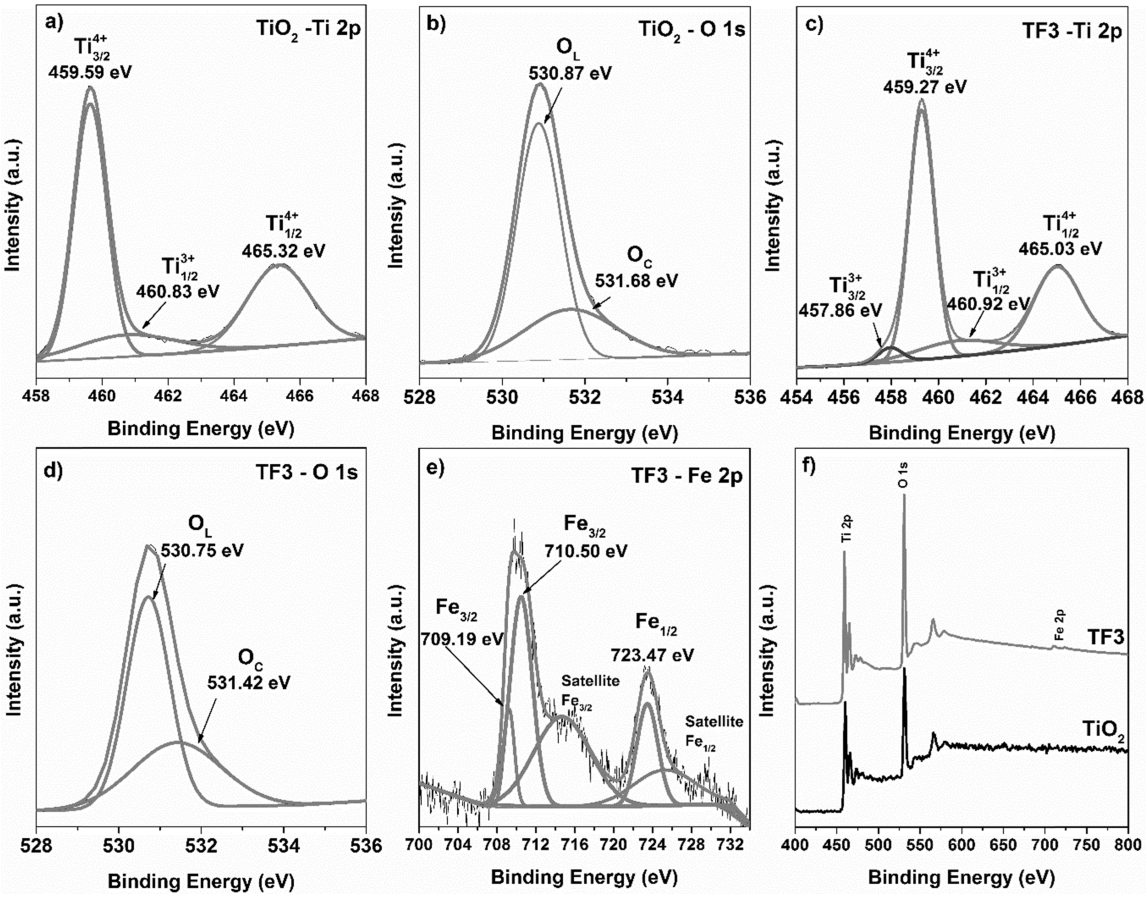

Fig. 6. XPS curves of Ti 2p, O 1s, and Fe 2p from the samples TiO_2 (a-b) and TF3 (c-e) image f shows the surveys of same both samples.

However, the sample TF3 (Fig. 6c) presents the Ti^{4+} state at 459.2 and 465 eV, and an extra peak corresponding to the Ti^{3+} state at 457.8 eV. It is suggested that the new state arises from the substitution of Ti^{4+} by Fe^{3+} ion. Hence, charge neutrality requires the formation of Ti interstitials of the lower valance [26]. Fig. 6b and 6d show the corresponding O 1s spectra. The two fitted peaks are assigned to the lattice oxygen atoms in the TiO_2 crystal. The peak at 530.8 eV on TiO_2 and 530.7 eV on TF3 are originated from the O-Ti and Fe-O bonds (O_L). The small second peak at 531.6 eV (also, 531.4 eV for TF3) might be originated from the hydroxyl groups and chemisorbed species (O_c) [27]. Additionally, analysis on Fe 2p was performed to confirm the effective doping (Fig. 6e). The plot exposes the binding energy of $2p_{3/2}$ at 709.1 for Fe^{2+} and 710.5 for Fe^{3+}. This information suggests the presence of bonds of the type Fe-O-Fe and Ti-O-Fe [28]. The survey spectra confirm the Ti, O, and Fe elements in the samples (Fig. 6f). In addition, the XPS suggests the existence of Ti^{4+}, Ti^{3+}, O, Fe^{2+}, and Fe^{3+} species in the samples.

Fig. 7 presents the Raman spectra of the as-prepared samples. The active vibrational modes were observed at 137.64 cm^{-1} (E_g), 391.6 cm^{-1} (B_{1g}), 507.5 cm^{-1} (A_{1g}), and 632 cm^{-1} (E_{2g}). All active modes are attributed to the anatase phase [29]. This information is consistent with the XRD results shown in Fig. 1. Nonetheless, it is evident that the intensity of the vibrational bond is decreased in the doped samples, and that is strongly dependent on the doping amount. These results can be

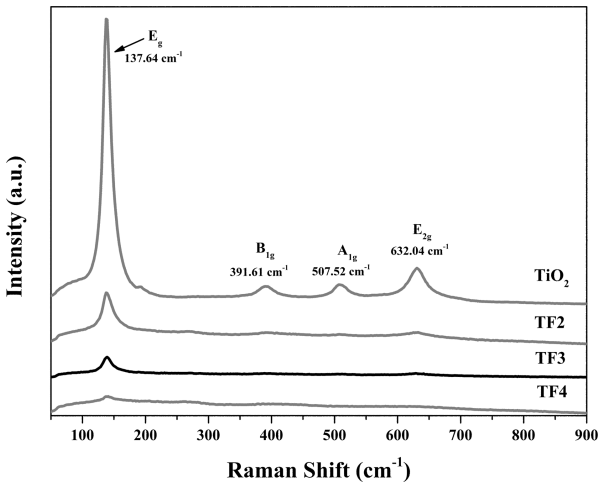

Fig. 7. Raman spectra of the as-prepared samples.

interpreted by the change of equilibrium in the lattice parameters, due to the substitution of Ti^{4+} by Fe^{3+}. This is, the difference in charge produces the enlargement and contraction of the crystal lattice leading to a decrease in the intensity of the peaks [30]. These results are in good accordance with the XPS analysis (Fig. 6).

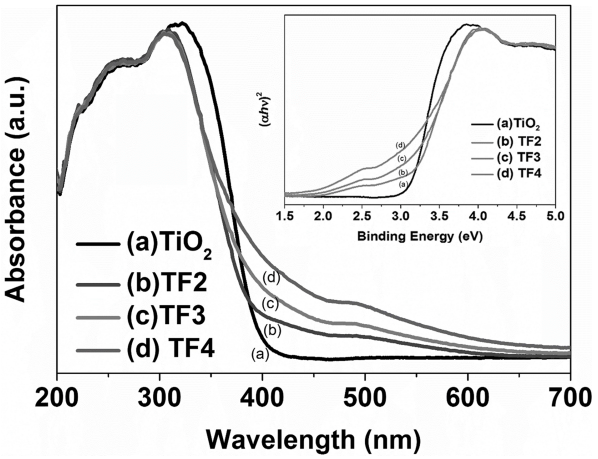

Fig. 8. UV-vis DRS UV absorption curves from the synthetized samples. Inset the corresponding Kubelka-Munk plots.

Optical properties were analyzed by DRS UV-Vis absorption. Fig. 8 presents the spectra corresponding to the as-synthesized samples. It is observed that the light absorption by samples lies in the UV region. However, the Fe-doped samples present an extra absorption peak at 500 to 600 nm (yellow color region). The change of coloration is related with the Jahn-teller split ($^2T_2 \rightarrow {}^2E$) electronic transitions. This transition is derived from the Ti^{3+} centers [31]. The visible light absorption range corresponds to the coloration of the powders. Later, the optical band-gap was obtained by the study of Kubelka-Munk Function [$(\alpha h\nu)^2$ vs hν], as shown in Fig. 8 (inset). Pure TiO_2 counts with a band gap of 3.1 eV. Likewise, TF2, TF3, and TF4 own bandgaps of 3.1, 2.7, and 2.6 eV, respectively. Hence, it is assumed that the Fe-doping decreases the band gap energy due to the new energy levels introduced by Fe ions between valance and conduction band [32]. To confirm this assumption, valance band-XPS analysis were performed.

Fig. 9 shows the XPS valance band curves corresponding to TiO_2 (Fig. 9a) and TF3 (Fig. 9b). Additionally, the

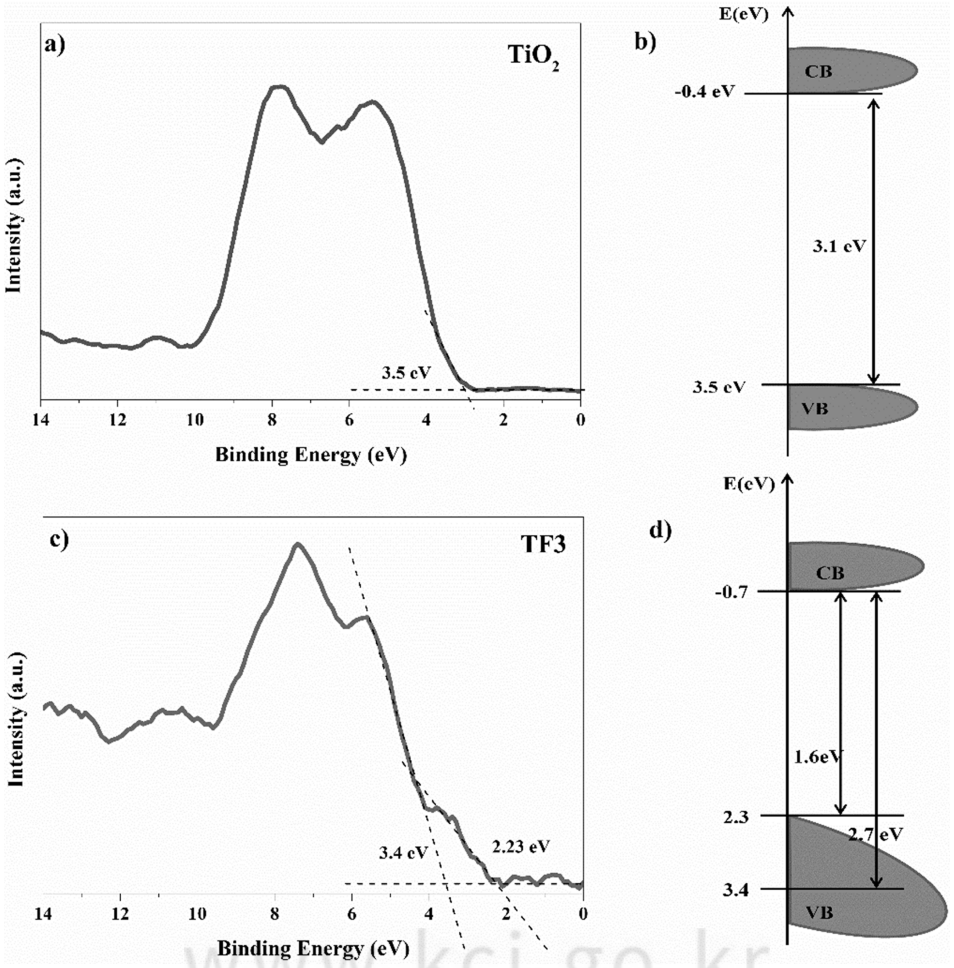

Fig. 9. VB-XPS plots along their suggested band-edge of the samples TiO_2 and TF3.

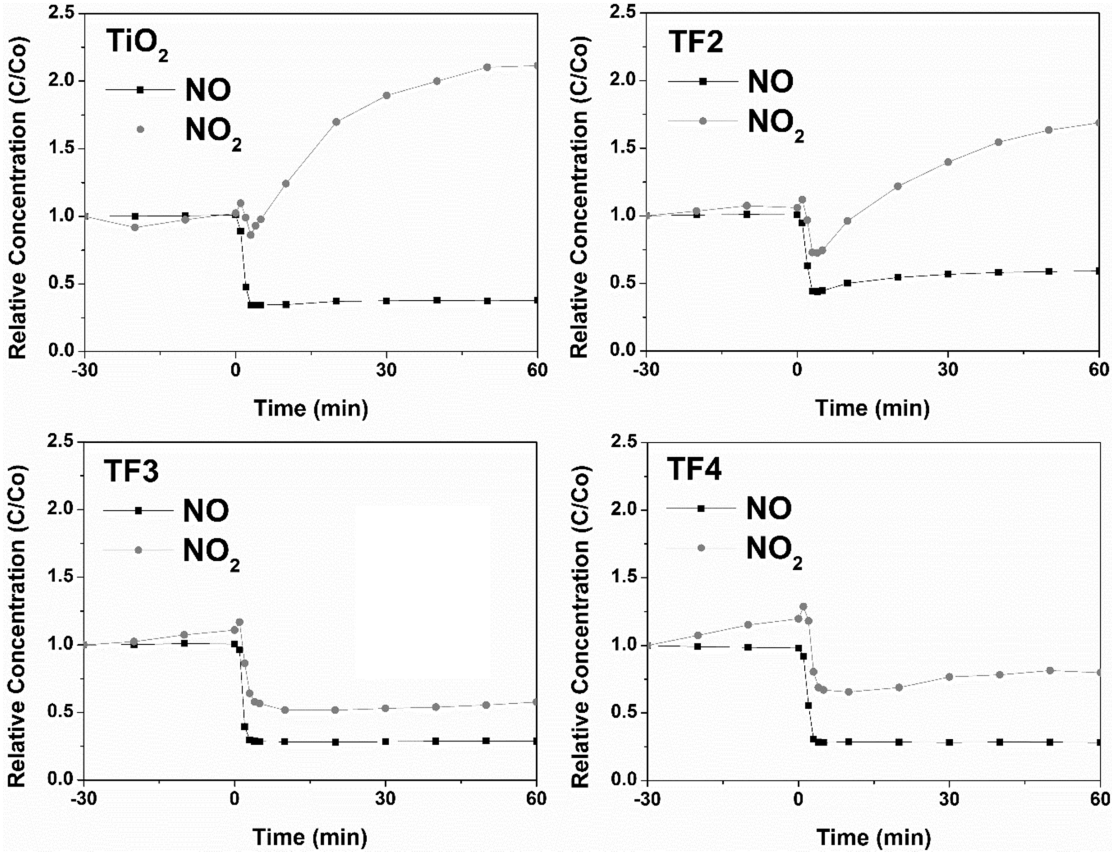

Fig. 10. DeNOx patterns of the samples TiO_2, TF2, TF3, and TF4.

proposed band edges on basis of the VB-XPS and the Kubelka-Munk information are shown. It is clear that the band gap of TF3 is reduced in comparison to TiO_2. Also, the band edge of TF3 manifests a new energy level observed at 0.9 eV above the valance band edge. The new level can be attributed to the unoccupied Ti^{3+} states formed by the introduction of Fe (III) and Fe (II) species [33].

Photocatalytic activity

Fig. 10 shows the oxidation process of the gaseous pollutant (NO) by the samples in presence of simulated solar light. The first 30 min corresponds to the DeNOx activity of the samples under dark conditions. After the light is turned on, an immediate decrease of NO is obtained until reaching concentration of ~70 % from the initial concentration. However, after the first 5 min, the samples TiO_2 and TF1 present an increased production of the NO_2, with above 2 times the initial concentration. The samples TF3 and TF4 show a different behavior, and after the first minutes of oxidation, NO_2 preserves a steady concentration of ~50 % of the initial value. Hence, the photo-oxidation efficiencies of TiO_2, TF2, TF3, and TF4 samples over DeNOx are 36 %, 40 %, 75 %, and 72 %, respectively. The results suggest that TF3 sample has better NOx oxidation tendency than others. The small particle size of ~10 nm with the large surface area of 283.99 m^2/g and a great amount of active sites are ascribed to the higher efficiency of TF3 sample. In the other words, the enhancement of NOx oxidation by Fe-doped TiO_2 is associated with low recombination of e^-/h^+ pairs due to the modification of the physicochemical and optical properties of the catalyst nanoparticles. The photocatalytic oxidation of NOx is attributed to the direct reaction with the radicals of type OH^- and $O_2^{-\bullet}$. Fig. 11 describes the proposed deNOx mechanism. The main process undergoes three sub-states ($NO \rightarrow NO_2 \rightarrow HNO_3 \rightarrow NO_3^-$). The oxidation of NO can happen through the adsorption of O_2^- and transformation of NO_3^-. Also, it can be achieved through the adsorption of the hydroxyl radicals ($OH^\bullet$) and transformation into NO_2 and then NO_3^- [34-36]. To support this information, Combustion Ion Chromatography studies were performed to confirm the production of NO_3^- ions at the catalyst surface. TF3 sample had the major production of 5346.4 μg/L followed by TF4 with 3909.2 μg/L, then TF2 with 414.9 μg/L and TiO_2 of 315.4 μg/L. These results are in good accordance with the degradation pathways in Fig. 10, where TF3 shows the lowest production of the toxic intermediate NO_2, followed by TF4, then TF2 and finally TiO_2.

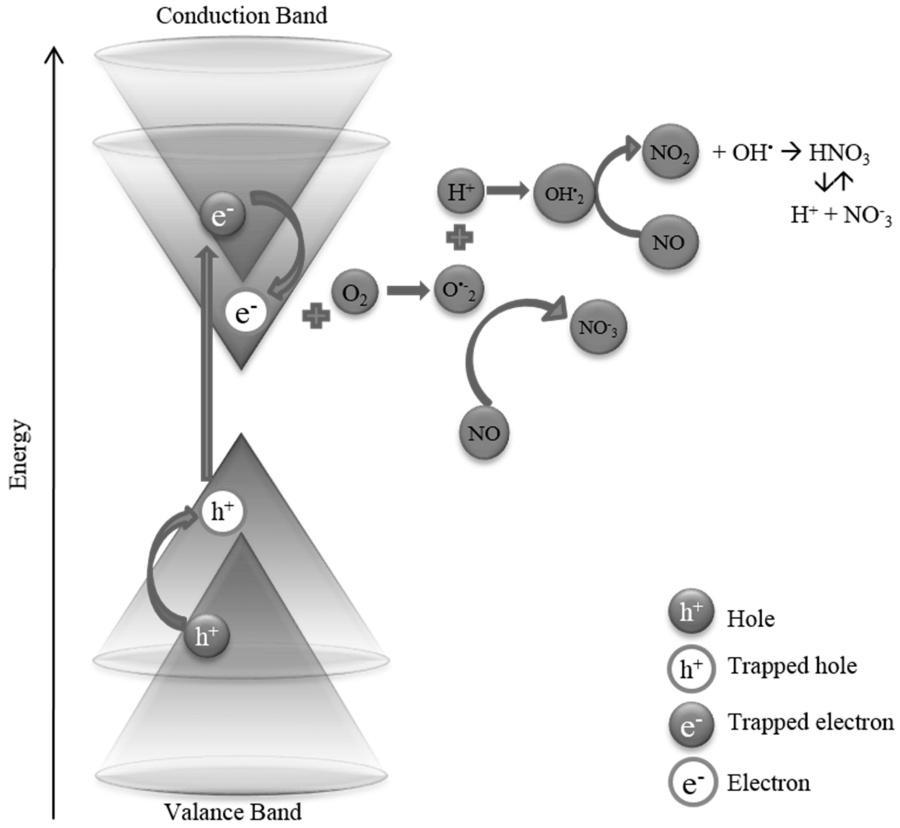

Fig. 11. The proposed photo-oxidation process of NOx gases.

Conclusions

The Fe doped TiO_2 samples were synthesized by a microwave hydrothermal-assited sol-gel process. The studies revealed the presence of anatase phase in the synthesized TiO_2 samples. The nanoparticles were successfully applied for the photocatalytic NOx removal. The TiO_2 doped with 3 mol% of Fe has shown an excellent performance to remove 75 % of NOx within 60 min without the production of the harmful NO_2 Intermediate. The outstanding performance is attributed to the modification on the physicochemical and optical properties of the catalyst by Fe doping. Moreover, the small particle size of ~10 nm promoted the large surface area of 283.99 m^2/g and a great amount of active sites. The changes in the chemical composition give rise to oxygen vacancies that act as e^-/h^+ trappers to produce active radicals. Added to this, the addition of Fe ions into the structure improved the light harvesting with a narrow bandgap of 2.8 eV. Hence, the study suggests that the Fe-doped TiO_2 nanoparticles via microwave hydrothermal-assisted sol-gel method can be a potential alternative for effective removal of NOx.

Acknowledgements

This Research was supported by the Global Research Laboratory Program of the National Research Foundation of Korea (NRF) funded by the Ministry of Education, Science and Technology (MEST) of Korea (Grant Number: 010-00339).

References

1. Environmental Protection Agency (EPA), Nitrogen oxides (NOx), why and how they are controlled, Epa-456/F-99-006R. (1999) 48.
2. J. Lasek, Y.-H. Yu, J.C.S. Wu, Removal of NOx by photocatalytic processes, J. Photochem. Photobiol. C Photochem. Rev. 14 (2013) 29-52.
3. J.J. Kaczur, Oxidation chemistry of chloric acid in NOx/SOx and air toxic metal removal from gas streams, Environ. Prog. 15 (1996) 245-254.
4. U.S. Environmental Protection Agency, Nitrogen Oxides Emissions, (2014) 23.
5. M.S. Solanki, S. Benjamin, Photocatalysis, Adv. Oxid. Process. Waste Water Treat. (2018) 135-175.
6. D. Ravelli, D. Dondi, M. Fagnoni, A. Albini, Photocatalysis. A multi-faceted concept for green chemistry, Chem. Soc. Rev. 38 (2009) 1999-2011.
7. T. Luttrell, S. Halpegamage, J. Tao, A. Kramer, E. Sutter, M. Batzill, Why is anatase a better photocatalyst than rutile? - Model studies on epitaxial TiO2 films, Sci. Rep. 4 (2015) 4043.
8. A. Fujishima, T.N. Rao, D.A. Tryk, Titanium dioxide photocatalysis, J. Photochem. Photobiol. C Photochem. Rev. 1 (2000) 1-21.
9. L.M. S. George, S. Pokhrel, Z. Ji, B. L. Henderson, T. Xia, L. J. Li, J. I. Zink, A. E. Nel, Role of Fe doping in tuning

the band gap energy of titanium dioxide for studying the light activated cytotoxicity, J. Am. Chem. Soc. 133 (2011) 11270-11278.
10. R. Jaiswal, J. Bharambe, N. Patel, A. Dashora, D.C. Kothari, A. Miotello, Copper and Nitrogen co-doped TiO_2 photocatalyst with enhanced optical absorption and catalytic activity, Appl. Catal. B Environ. 168-169 (2015) 333-341.
11. M.B. Suwarnkar, R.S. Dhabbe, A.N. Kadam, K.M. Garadkar, Enhanced photocatalytic activity of Ag doped TiO_2 nanoparticles synthesized by a microwave assisted method, Ceram. Int. 40 (2014) 5489-5496.
12. Y.-H. Peng, G.-F. Huang, W.-Q. Huang, Visible-light absorption and photocatalytic activity of Cr-doped TiO_2 nanocrystal films, Adv. Powder Technol. 23 (2012) 8-12.
13. Q.R. Deng, X.H. Xia, M.L. Guo, Y. Gao, G. Shao, Mn-doped TiO_2 nanopowders with remarkable visible light photocatalytic activity, Mater. Lett. 65 (2011) 2051-2054.
14. I. Ganesh, P.P. Kumar, I. Annapoorna, J.M. Sumliner, M. Ramakrishna, N.Y. Hebalkar, G. Padmanabham, G. Sundararajan, Preparation and characterization of Cu-doped TiO_2 materials for electrochemical, photoelectrochemical, and photocatalytic applications, Appl. Surf. Sci. 293 (2014) 229-247.
15. R. Ribeiro, S. de Lazaro, C. de Oliveira, Band-Gap Engineering for Photocatalytic Applications: Anionic and Cationic Doping of TiO_2 Anatase, Curr. Phys. Chem. 6 (2016) 22-27.
16. Y. Zhang, Q. Li, Synthesis and characterization of Fe-doped TiO_2 films by electrophoretic method and its photocatalytic activity toward methyl orange, Solid State Sci. 16 (2013) 16-20.
17. N.H. Hao, G. Gyawali, S.W. Lee, Ceramic Processing Research Rapid synthesis of TiO_2 nanotubes via microwave-assisted hydrothermal method, J. Ceram Process Res. 18 (2017) 36-40.
18. S. Narakaew, The nano-TiO_2 synthesis using ultrasonic assisted sol-gel method and its photocatalytic degradation of methylene blue, J. Ceram Process Res. 17 (2016) 409-413.
19. A. Monshi, M.R. Foroughi, M.R. Monshi, Modified Scherrer Equation to Estimate More Accurately Nano-Crystallite Size Using XRD, World J. Nano Sci. Eng. 02 (2012) 154-160.
20. M. Hinojosa-Reyes, V. Rodríguez-González, R. Zanella, Gold nanoparticles supported on TiO_2 -Ni as catalysts for hydrogen purification via water-gas shift reaction, RSC Adv. 4 (2014) 4308-4316.
21. Y. Yang, Y. Yu, J. Wang, W. Zheng, Y. Cao, Doping and transformation mechanisms of Fe^{3+} ions in Fe-doped TiO_2, CrystEngComm. 19 (2017) 1100-1105.
22. B.I. Kidyarov, N.D. Dandaron, Kinetics of non-stationary nucleation in solutions, J. Cryst. Growth. 52 (1981) 812-815.
23. A. Chianese, F. Di Berardino, A.G. Jones, On the effect of secondary nucleation on the crystal size distribution from a seeded batch crystallizer, Chem. Eng. Sci. 48 (1993) 551-560.
24. M. Thommes, Physical adsorption characterization of nanoporous materials, Chemie-Ingenieur-Technik. 82 (2010) 1059-1073.
25. B. Viswanathan, K.J.A. Raj, Effect of surface area, pore volume and particle size of P25 titania on the phase transformation of anatase to rutile, Indian J. Chem. - Sect. A Inorganic, Phys. Theor. Anal. Chem. 48 (2009) 1378-1382.
26. Y. Duan, N. Fu, Q. Liu, Y. Fang, X. Zhou, J. Zhang, Y. Lin, Sn-doped TiO_2 photoanode for dye-sensitized solar cells, J. Phys. Chem. C. 116 (2012) 8888-8893.
27. X. Jiang, Y. Zhang, J. Jiang, Y. Rong, Y. Wang, Y. Wu, C. Pan, Characterization of Oxygen Vacancies Associates within the Hydrogenated TiO_2 : a Positron Annihilation Study Characterization of Oxygen Vacancies Associates within the Hydrogenated TiO_2 : a Positron Annihilation Study, J.Phys.Chem.C. 116 (2012) 22619-22624.
28. P. Li, E.Y. Jiang, H.L. Bai, Fabrication of ultrathin epitaxial γ-Fe_2O_3 films by reactive sputtering, J. Phys. D. Appl. Phys. 44 (2011) 075003.
29. T. Ohsaka, F. Izumi, Y. Fujiki, Raman spectrum of anatase, TiO_2, J. Raman Spectrosc. 7 (1978) 321-324.
30. A. Das, S. Pisana, B. Chakraborty, S. Piscanec, S.K. Saha, U. V. Waghmare, K.S. Novoselov, H.R. Krishnamurthy, A.K. Geim, A.C. Ferrari, A.K. Sood, Monitoring dopants by Raman scattering in an electrochemically top-gated graphene transistor, Nat. Nanotechnol. 3 (2008) 210-215.
31. N. Serpone, C. Organica, V. Uni, V. Taramelli, V. Pa, Is the Band Gap of Pristine TiO_2 Narrowed by Anion- and Cation-Doping of Titanium Dioxide in Second-Generation Photocatalysts?, J. Phys. Chem. B. 110 (2006) 24287-24293.
32. C.H. Wu, Effects of operational parameters on the decolorization of C.I. Reactive Red 198 in UV/TiO_2-based systems, Dye. Pigment. 77 (2008) 31-38.
33. A.G. Thomas, W.R. Flavell, A.R. Kumarasinghe, A.K. Mallick, D. Tsoutsou, G.C. Smith, R. Stockbauer, S. Patel, M. Grätzel, R. Hengerer, Resonant photoemission of anatase TiO_2 (101) and (001) single crystals, Phys. Rev. B. 67 (2003) 035110.
34. J.. Dalton, P.. Janes, N.. Jones, J.. Nicholson, K.. Hallam, G.. Allen, Photocatalytic oxidation of NOx gases using TiO_2: a surface spectroscopic approach, Environ. Pollut. 120 (2002) 415-422.
35. J. Ma, H. Wu, Y. Liu, H. He, Photocatalytic Removal of NOx over Visible Light Responsive Oxygen-Deficient TiO_2, J. Phys. Chem. C. 118 (2014) 7434-7441.
36. H. Wang, Z. Wu, W. Zhao, B. Guan, Photocatalytic oxidation of nitrogen oxides using TiO_2 loading on woven glass fabric, Chemosphere. 66 (2007) 185-190.